Acta Materialia 242 (2023) 118433

Contents lists available at ScienceDirect

Acta Materialia

journal homepage: www.elsevier.com/locate/actamat

Full length article

Kinetics and evolution of solid-state metal dealloying in thin films with multimodal analysis

Chonghang Zhao[a,c], Lin-Chieh Yu[a,b], Kim Kisslinger[d], Charles Clark[a], Cheng-Chu Chung[a], Ruipeng Li[c], Masafumi Fukuto[c], Ming Lu[d], Jianming Bai[c], Xiaoyang Liu[a], Hui Zhong[e], Mingzhao Liu[d], Sanjit Ghose[c], Yu-chen Karen Chen-Wiegart[a,c,*]

[a] Department of Materials Science and Chemical Engineering, Stony Brook University, Stony Brook, NY 11794, USA
[b] Department of Chemistry, Stony Brook University, Stony Brook, NY 11794, USA
[c] National Synchrotron Light Source II, Brookhaven National Laboratory, Upton, NY 11973, USA
[d] Center for Functional Nanomaterials, Brookhaven National Laboratory, Upton, NY 11973, USA
[e] Department of Joint Photon Science Institute, Stony Brook University, Stony Brook, NY 11794, USA

ARTICLE INFO

Article history:
Received 30 August 2021
Revised 7 October 2022
Accepted 12 October 2022
Available online 13 October 2022

ABSTRACT

Thin-film solid-state metal dealloying (thin-film SSMD) is an emerging technique that uses self-organization to design nanostructured thin films. The resulting 3D bicontinuous nanostructures are promising for a wide range of applications, such as catalysis and energy storage. In this work, we prepared thin films by SSMD using Ti-Cu as the parent alloy and Mg as the solvent. Using a multimodal approach, we combined synchrotron X-ray spectroscopy, diffraction, and high-resolution electron-based spectroscopy and imaging to study their morphological, structural, and chemical evolution. The processing-structure relationship was analyzed as a function of parent alloy composition and dealloying temperature and time. Morphological transitions from globular, to lamellar, to bicontinuous structures, in conjunction with a ligament size evolution, were identified as functions of the parent alloy composition. The dealloying rate increased with increasing concentration of interdiffusing elements (dissolving component) in the parent alloy. The parting limit, a dealloying compositional threshold, was systematically analyzed and determined to be 30%–40%. The order of crystalline phase formation is $CuMg_2$, Cu_2Mg, and Ti; the Ti phase first shows self-reorganization during dealloying, separate from the crystallization process. The coarsening in thin-film SSMD was identified and not entirely self-similar; in addition to the increase of ligament size over time, the formation of larger globular ligaments were also observed. This work furthers our fundamental understanding of thin-film SSMD and nanostructured thin-film design, where the thermodynamic and kinetic effects differ from the bulk counterparts. The fact that dealloying and diffusion outpaces the crystallization and new phase formation also offers opportunities to utilize thin-film SSMD in certain alloy systems in which deleterious intermetallic phases need to be suppressed, that may not be possible in the bulk geometry.

1. Introduction

Nanoporous metals and their unique properties, including high surface-area-to-volume ratios, light weights, chemical reactivities, and high thermal and electrical conductivities, have received great attention [1–3]. Dealloying by selective removal of component(s) from a parent alloy and self-arrangement by the remaining components to form a bicontinuous structure [4] are effective methods for fabricating nanoporous metals [5,6]. Dealloying has been applied to fabricate materials for numerous applications, including catalysts [6–9], hydrophilic substrates [10], sensors [11], and energy storage materials [12–15] Depending on the type of dealloying agents and conditions, dealloying methods can be categorized as aqueous solution dealloying (ASD), metal-agent dealloying, molten salt dealloying (MSD), and vapor phase dealloying (VPD). ASD, [16] using an aqueous solution as a solvent, requires sufficient redox potential differences between the elements in the parent alloy and has been widely applied to fabricate nanoporous noble metals and metal oxides [17,18]. VPD, using a saturated vapor pressure difference between constituent components in a parent alloy, has been applied to fabricate various nanoporous metals, including Ti, Ni, Si, and Cu, from zinc-based parent alloys [19,20]. MSD, using a bath of molten salt as the solvent, was introduced as a green method to fabricate porous materials [21].

* Corresponding author.
E-mail address: Karen.Chen-Wiegart@stonybrook.edu (Y.-c.K. Chen-Wiegart).

https://doi.org/10.1016/j.actamat.2022.118433
1359-6454/

Metal-agent dealloying utilizes metal as the solvent to introduce dealloying. Depending on whether the metallic solvent is in a liquid or solid state, it can be categorized as liquid metal dealloying (LMD) or solid metal dealloying. LMD uses a liquid metal as the solvent, and the dealloying process is primarily driven by the mixing enthalpy difference between the parent alloy and solvent to fabricate less noble nanoporous materials [22]. LMD has been used to fabricate a wide range of nanoporous materials, including silicon [23], stainless steel [24,25], magnesium [26], graphite [27], α-titanium [22,28], β-titanium [29], copper [30,31], zirconium [31], niobium [32], tantalum [32–34], titanium zirconium alloys [35], and TiVNbMoTa high-entropy alloys [36]. Recently, SSMD, also known as solid-state interfacial dealloying (SSID), using a solid-state metal as a solvent to drive the dealloying process, has been introduced to fabricate nanoporous Fe, Fe-Cr, Ti [37–39], and nanocomposites with ever-finer ligament size [40]. Thin-film SSMD, which applies SSMD to a thin-film geometry, has been recently demonstrated [41]. It uses thinner layers that allow the use of shorter dealloying times to fabricate finer features than those obtained by applying SSMD to bulk structures and makes it possible to combine SSMD with a range of substrates for functional applications.

Fundamental understanding of kinetics and pattern formation has provided insights into the underlying mechanisms of dealloying. In ASD, the mechanisms of nanoporosity evolution and ligament coarsening were systematically studied [4,14,42,43]. The parting limit, a compositional threshold for dealloying full structures, was explained by percolation theory [44,45]. Atomistic simulations, including kinetic Monte Carlo simulations [46,47], molecular dynamics simulations [48,49], and continuum simulations such as phase-field modeling [48], were applied to simulate morphological evolution during dealloying. Kinetics studies in LMD were developed by partially adapting theories from ASD. Geslin et al. and Lai et al. applied phase-field simulation modeling to identify morphological evolution during LMD [50,51], including the formation of unique filaments and globular ligaments. McCue et al. developed a kinetics model for LMD and predicted the kinetics of selective dissolution and morphological evolution [33]. Joo and Kato determined the influence of dealloying temperature and rate on the phase transformation and analyzed the relationship between precursor crystal structure and ligament structure generated by LMD [52,53]. Zhang et al. analyzed the kinetics in SSMD and correlated the evolution in ligament size with changes in mechanical properties [54]. McCue and Demkowicz tested the alloy design criteria for SSMD in thin films and proposed that volume changes hindered thin-film SSMD processes [40]. However, the details of the material kinetics during the morphological evolution and phase transformation of SSMD remain unexplored. Providing such knowledge is a critical step toward understanding the process-structure-property relationship for material design. Notably, three aspects of the material design may exhibit heterogeneity, all of which play critical roles in determining the ultimate functionalities of the materials: (1) *morphology,* including feature size and shape; (2) *crystal structure:* phase identification, structural change, and crystallization; and (3) *chemistry:* phase composition, phase separation, dealloying propagation, and residuals [33,42,55–58]. Only by understanding the morphological, structural, and chemical evolution of SSMD and the conditions that can lead to this unique bicontinuous structure can we tailor the synthesis process to create materials with specific structures and compositions.

In this work, we systematically analyzed the kinetics of SSMD in thin films (thin-film SSMD) with Ti-Cu as the parent alloy and Mg as the solvent. Processing parameters including the parent alloy composition (10 at.%–90 at.% Ti), dealloying time (7.5, 15, 30 and/or 60 min, depending on the dealloying temperature), and dealloying temperature (340, 400, and 460 °C) were investigated. Synchrotron X-ray diffraction (XRD), Grazing-Incidence Wide-angle X-ray scattering (GIWAXS), and extended X-ray absorption fine structure (EXAFS) spectroscopy were applied to reveal the structural and chemical evolution during thin-film SSMD. Cross-sectional scanning electron microscopy (SEM) and scanning transmission electron microscopy/energy-dispersive X-ray spectroscopy (STEM/EDX) were applied to understand the morphological evolution of Ti ligaments generated by dealloying. The crystallization of TiCu parent alloy, Ti, Cu_2Mg, and $CuMg_2$ phases were identified as a function of dealloying time, temperature, and parent alloy composition. The parting limit was identified in Ti-Cu as 30–40 at.%. The diffusion-coupled growth, and the coarsening of ligaments at the later stage were analyzed, which explained the ligament shape and size transition with the varying parent alloy composition. The diffusion rate variations in thin-film SSMD were identified, which were associated with the different parent alloy compositions. Overall, this study furthered our understanding of the processing-structural/morphological/chemical relation in designing materials by thin-film SSMD, which can be applied to a wider range of elemental selection for functional applications such as catalysts and energy storage materials.

2. Materials and methods

Thin-film SSMD samples were prepared at the Center for Functional Nanomaterials (CFN), Brookhaven National Laboratory (BNL). Borosilicate glass slides (Ted Pella) with 1×1 cm^2 area and ~170 μm thickness were used as substrates for deposition. Before deposition, the surfaces of the glass slides were cleaned with isopropyl alcohol and deionized water and then an oxygen plasma treatment. Ta thin films were formed by sputtering deposition (the sputtering target was 99.95% purity from Kurt J. Lesker) as a barrier layer. Ti_xCu_{1-x} alloy thin films (x=10–90 at.% with a 10 at.% increment, 99.95% purity from Stanford Advanced Materials) and Mg thin film (99.95% purity from Kurt J Lesker and Stanford Advanced Materials) were prepared by sputtering deposition as parent alloys and solvent, respectively. Each of the sputtering targets was pre-sputtered for 5–10 min to remove surface oxides before opening the sputtering shutter. Ta, Ti-Cu, and Mg films were sequentially sputtered onto glass slides. The film thicknesses were ~80 nm for Ta, ~300 nm for Ti-Cu, and ~500 nm for Mg, as measured by focused ion beam-scanning electron microscopy (FIB-SEM, Helios dual beam, FEI) cross-sectional imaging. Note that the film thicknesses and the substrate materials are different from our previously reported work [39].

The deposited multilayer thin-film samples were heated by rapid thermal processing (Modular Process Technology Corp., model number RTP-600S) for isothermal heat treatment to perform solid-state metal dealloying. All heat treatments were conducted in a reducing gas atmosphere (4% hydrogen and 96% argon) to prevent oxidation. Samples were heated from ambient temperature to the designated temperature in 30 s and held for a designated duration. The samples were then cooled to ambient temperature in 150 s. The heating temperature and time were determined, based on the diffusion length $l = \sqrt{2Dt}$ using diffusion data in the literature, such that the interdiffusion length between the solvent and the interdiffusing elements (dissolving component) was greater than the thickness of the parent alloy film [59]. Note that this is likely an under-estimate on the distance of the dealloying front propagation, if the process is instead dominated by interfacial phenomena such as the surface diffusion or the reaction at the interfaces. Although RTP provides a relatively accurate time control on annealing, especially for shorter dealloying times, it is not designed maintain a prolonged heat treatment time. To keep the annealing condition consistent, this study focuses on studying dealloying at the early stage. A 30 min treatment as the upper bound

of the annealing time was verified experimentally to be sufficient to introduce chemical and morphological changes for the temperature range used in this study. The shortest annealing time used was 7.5 min, considering both the diffusion length noted above, and practically to keep an accurate dealloying time measurement considering the ramping (30 s) and cooling time of the instrument. Additionally, the annealing temperature was kept within a relatively narrow range (340–460 °C) to study the consistent mechanism governing the morphological and phase changes; also using a much lower annealing temperature will require a much longer annealing time to observe similar changes in the samples, which was not possible due to the limits of the RTP method, as explained.

FIB-SEM was used to obtain cross-sectional SEM images. A machine-learning-based segmentation package, Weka [60] in ImageJ, was applied to segment the Ti-rich and Cu-Mg-rich regions in the cross-sectional images. The feature size distributions were quantified on segmented images using a customized MATLAB program developed in-house following an established method [61]. The ligament size quantification with parent alloy composition was processed on segmented cross-sectional SEM images, as shown in Fig. S1. The STEM lamella sample was prepared by FIB-SEM following a standard procedure with a thickness less than 100 nm for electron transparency. STEM characterization was carried out with STEM (Talos, FEI) operated at 200 keV. High-angle annular dark-field imaging (HAADF) and energy-dispersive spectroscopy (EDX) measurements were conducted. Both the FIB-SEM and STEM-EDX characterizations were performed at the CFN, BNL.

Synchrotron X-ray diffraction measurements were conducted at the X-ray powder diffraction beamline (XPD, 28-ID) at National Synchrotron Light Source II (NSLS-II, Brookhaven National Laboratory, BNL). The incident X-ray beam energy was 64.187 keV, with a corresponding X-ray wavelength of 0.19316 Å. The beam size was 0.5 mm×0.5 mm. A large-area X-ray detector with 2048×2048 pixels was used to collect the diffraction patterns, and the size of each pixel was 200×200 μm^2. The distance from the sample to the detector was 1378.43 mm, calibrated with a Ni standard. Phase identification was carried out by comparing peak locations with references using commercial software packages (Jade 9, Materials Data, Inc.) The peak area intensity of each of the identified phases was determined using a Python program developed in-house. The peak area was calculated by integrating the area under the XRD curve after subtracting a linear background.

Synchrotron X-ray absorption spectroscopy at the Ti K-edge and Cu K-edge was conducted at the Beamline for Materials Measurement (BMM, 6-BM) at NSLS-II, BNL. The spectra were collected in fluorescence mode at a glancing angle of 3º. Cu and Ti foils and standard powders, including Ti(II)O, Ti(III)$_2$O$_3$, Ti(IV)O$_2$ rutile, CuO, and Cu$_2$O (Sigma Aldrich), were measured in transmission mode. Eight scans of each sample were collected and averaged to improve the signal-to-noise ratio. The averaging, energy calibration, normalization and background subtraction of the X-ray absorption spectroscopy (XAS) spectra were conducted with Athena software [62]. The energy was calibrated to the first derivative peaks in metallic Ti at 4966.0 eV and Cu at 8979.0 eV. Linear regression was conducted to fit the pre-edge region, and a quadratic polynomial was used to fit the post-edge region. Background removal was performed using an *Rbkg* value of 1.0–1.4 and a *k* weight of 2 to reduce the low-radial distance component in the Fourier transform.

The EXAFS data were modeled using the Demeter data analysis package [62]. The fits were performed in *R* space using the theoretical EXAFS equation with photoelectron scattering amplitudes and phase shifts using FEFF6.2 in the Demeter package [63]. The fitting process was performed separately for Ti and Cu absorption edges by applying appropriate constraints between the fitting parameters. In the theoretical EXAFS signal, the coordination numbers (*CN*), bond distances (*R*), and mean-square-displacements (σ^2) were set as variables. The amplitude reduction factor values (S_0^2) were fixed for the same absorption edge in all spectra while the other parameters were varied. To model the Ti K-edge EXAFS, Ti-O, Ti-Cu, and Ti-Ti paths were included in the fitting model. The amplitude reduction factor ($S_0^2 = 0.539$) was determined by fitting the EXAFS spectra from the Ti standard foil. For the Cu K-edge EXAFS fits, Cu-Ti, Cu-Mg and Cu-Cu paths were included in the fitting model. The amplitude reduction factor ($S_0^2 = 0.814$) was determined by fitting the EXAFS spectra of the Cu standard foil. Depending on the quality of the data, the fitting range in *k* space was 2–8 Å^{-1} or 2–10 Å^{-1} for Ti and Cu; the fitting range in *R* space was 1–3 Å for Ti and 1–2.7 Å, 1–3 Å or 1.25–3 Å for Cu.

Grazing-Incidence Wide-Angle X-ray Scattering (GIWAXS) was performed at the Complex Materials Scattering beamline (CMS, 11-BM), NSLS-II at Brookhaven National Laboratory. The thin-film samples were placed at an incidence angle of 0.3° relative to the x-ray beam of 13.5 keV. The whole experiment was conducted in a vacuum to avoid background scattering from the air. The scattering data were collected by Pilatus800k detector placed 260 mm away from the sample with a 10 s exposure time. The sector-averaged profiles of GIWAXS data in *q* were extracted from the 2D detector *via* SciAnalysis and plotted in Python and Origin software for data visualization.

3. Results and discussion

3.1. Morphology transition with the parent alloy composition

Cross-sectional SEM views of dealloyed Ti$_x$Cu$_{1-x}$ layers (x = 10–90 at.% with a 10 at.% increment) at 460 °C for 30 min are shown in Fig. 1. For brevity, the samples are named following the convention of composition-temperature-time; for example, the parent alloy Ti$_{10}$Cu$_{90}$ at.% dealloyed at 460 °C for 30 min is denoted Ti$_{10}$Cu$_{90}$-460C-30. With increasing Ti concentration in the parent alloy, the morphology of Ti ligaments transitioned from globular to lamellar, bicontinuous, and finally, featureless. Such a morphological transition with parent alloy composition was also reported by phase-field simulations and experiments in LMD [50]. In the simulation of pattern formation in LMD, the morphology is controlled by interfacial spinodal decomposition and diffusion-coupled growth. In diffusion-coupled growth, the amount of remaining element determines whether diffusion-coupled growth continues to create a connected structure or a separate globular structure. In subsequent coarsening, surface diffusion pulls materials from saddle-point curvature ligaments and pinch-off ligaments, which are controlled by Rayleigh-Plateau instabilities [42,50]. Pinch-off ligaments decrease the structural connectivity and reduce the mechanical integrity of samples such that the dealloyed structure is only robust when the composition of the remaining element is above 30 at.% [33].

Considering that the mechanical integrity is mostly controlled by the shape and connectivity of the ligaments, it is important to discuss the relationship between the morphology and parent alloy composition. Note that here, the relationships between the morphological transitions and alloy composition differ in thin-film SSMD and LMD. In thin-film SSMD, globular Ti ligaments can be found in samples dealloyed from 20 at.% Ti in the parent alloy, and lamellar ligaments can be found in samples with 30–40 at.% Ti in the parent alloy. In LMD, a globular ligament was reported with 5 at.% of the remaining element, Ta, in the parent alloy, and a lamellar shape was found when 15 at.% of the remaining element Ta was in the parent alloy. This difference may not be attributed simply to the differences in the elements. Previously, Okulov et al. reported a bicontinuous structure created by dealloying a Ti$_{20}$Cu$_{80}$ alloy using liquid Mg (LMD method). Shi et al. also demonstrated dealloying the same alloy system to create a bicontinuous struc-

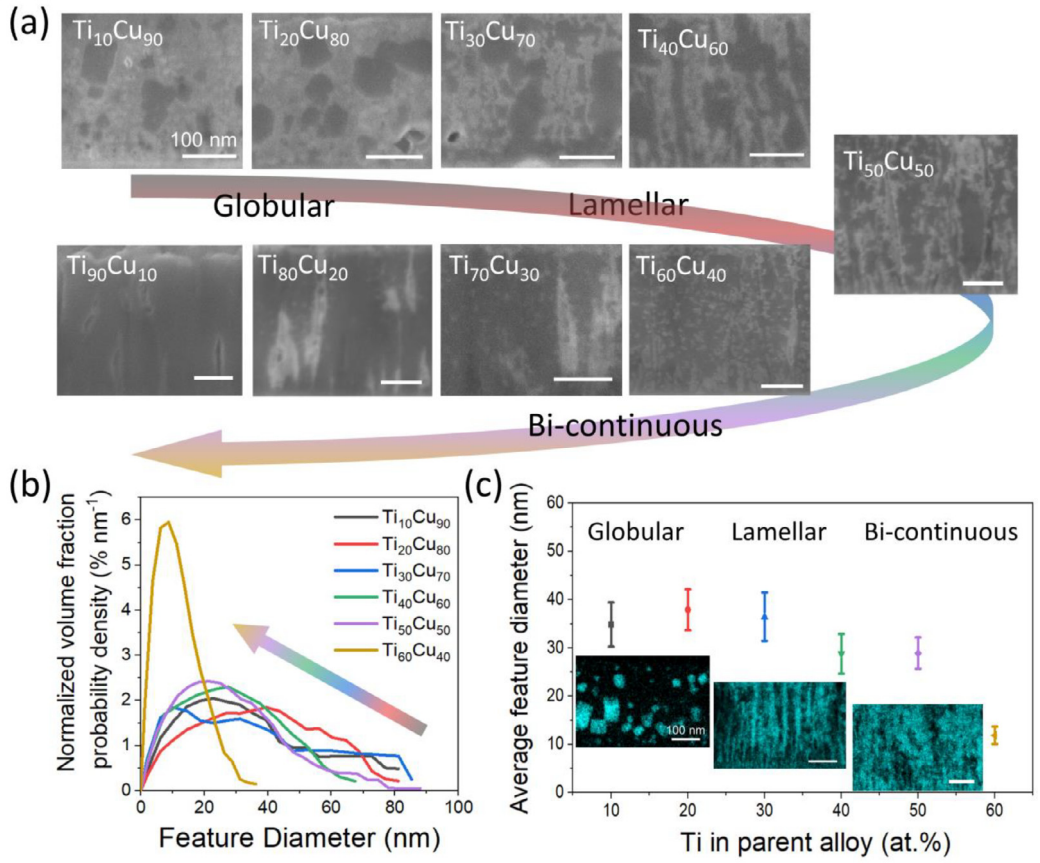

Fig. 1. The morphology, Ti ligament size distribution and corresponding average Ti ligament size of samples dealloyed from Ti_xCu_{1-x} (x = 10–60 at.%, with a 10 at. % increment) by Mg. All samples were dealloyed at 460 °C for 30 min. (a) Cross-sectional SEM view of Ti_xCu_{1-x} (x = 10–90 at.%, 10 at.% increment) dealloyed by Mg at 460 °C for 30 min, with Ti morphology transitions from globular to lamellar, to bicontinuous and featureless in the dealloyed samples. The dark gray regions correspond to the Ti-rich phase, and the light gray regions correspond to the Cu-Mg rich phase. (b) Ti ligament size distribution (the arrows indicate increasing amounts of Ti, the remaining element, in the parent alloy), (c) the average Ti ligament size with STEM/EDX maps of Ti showing the morphological transitions.

ture but using solid-state Mg as a solvent; however, the dealloying temperature used in their work was higher than the eutectic point of the $CuMg_2$ and Mg phases, and thus, the true reaction may not be a solid-state reaction [35,38]. The crystallinity of the sample was not reported in the LMD experiment with the Ti-Cu/Mg system, but the $TiCu_4$ and Ti_2Cu_3 phases are commonly identified as orthorhombic and tetragonal structures under ambient conditions; orthorhombic Cu_3Ti in the parent alloy was reported by Shi et al. in an SSMD experiment, while our parent alloy is amorphous. In contrast, McCue et al. applied SSMD to dealloy a $Ta_{15}Ti_{85}$ parent alloy thin film (~500 nm) using a bulk solid-state solvent, Zr, and reported a similar nonpercolating structure and an interpenetrating structure by dealloying $Ta_{25}Ti_{75}$ [64]. Their ligament shape transitions with parent alloy composition are closer to what is observed in this work. Such a difference in shape transitions with parent alloy composition may be related to a slow diffusion/self-reorganization process in the SSMD or the geometry in thin-film SSMD. The relative rates of dealloying interfacial movement and the dissolution of the interdiffusing elements (dissolving component) correlate with the connected morphology in dealloying [46]. In LMD, the rate-limiting process is interdiffusing elements dissolution, and slower dissolution provides more time for the remaining elements to reorganize and form a connected morphology. In SSMD, both the dissolution of the interdiffusing elements into the solid-state solvent and the self-organization of the remaining elements are slower than those in LMD. If the interfacial movement relative to the dissolution rate is lower in SSMD, then the formation of connected morphology can become more difficult than that by LMD; hence, it may require a higher atomic ratio for the remaining element to form a bicontinuous structure.

In addition to the Ti ligament morphological transition, the Ti ligament size also evolves as a function of the parent alloy composition. The Ti ligament size distribution and the corresponding average ligament size of the dealloyed samples *vs.* the parent alloy compositions are shown in Fig. 1(b) and (c). The analysis was based on segmented SEM images shown in Fig. S1. In samples dealloyed from the parent alloy with a lower concentration of the remaining element, Ti, a wider ligament size distribution was observed. With increasing amount of Ti in the parent alloy, a narrower Ti ligament size and smaller average size were observed. On the one hand, such variation in ligament-size distribution is related to differences in the coarsening mechanism. The large globular ligament is likely caused by the coarsening at the later stage, which influences the ligament size distribution. The coarsening is more limited in samples dealloyed from parent alloys with a higher concentration of Ti, so that their ligament size distribution becomes narrower, and their average sizes are smaller. This was most noticeable in the $Ti_{60}Cu_{40}$ sample. On the other hand, the rate-limiting process in dealloying may vary with parent alloy composition, and the dealloying rate varies. In LMD, the activation energy for the dealloying process varies with the parent alloy composition, and the rate-limiting process transitions from interdiffusing elements dissolution to residual element surface diffusion/reorganization [33]. Different dealloying rates in different parent alloys were also found by systematic XRD analysis, which will be discussed in a later section.

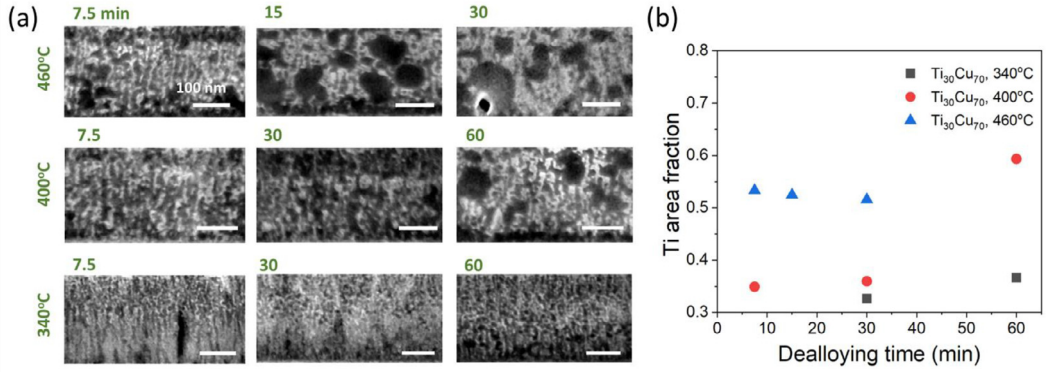

Fig. 2. (a) Cross-sectional SEM images of $Ti_{30}Cu_{70}$ dealloyed by Mg at 340, 400, and 460 °C from 7.5 min to 60 min. The images were cropped, and only the Ti/Cu_xMg dealloyed layer was present. All of the scale bars correspond to 100 nm. The dark gray regions correspond to the Ti-rich phase, and the light gray regions corresponds to the Cu-rich phase. (b) Area fraction of the Ti-rich phase evolution of $Ti_{30}Cu_{70}$ dealloyed by Mg at 340, 400, and 460 °C from7.5 min to 60 min.

3.2. Dealloying kinetics - morphology transition with dealloying time and temperature

The morphological and chemical evolution during dealloying are functions of the dealloying temperature and time. Here, we define the dealloying rate as the rate of removing dissolvable Cu from the parent alloy, and define complete dealloying as the dissolvable Cu having been completely removed from the parent alloy. We first analyzed the morphological evolution from the area fraction of the Ti-rich phase in cross-sectional SEM images. The chemical evolution with bonding type and atomic coordination were then analyzed by EXAFS. The Ti-rich phase area fraction shown in the analysis of the cross-sectional SEM images correlates to the Ti concentration in the sample and has been applied to analyze the dealloying progress [64]. EXAFS analysis was employed to further confirm the local chemical information at different dealloying stages.

The dealloying rate was analyzed in $Ti_{30}Cu_{70}$ samples, and their Ti-rich phase area fraction evolution is summarized in Fig. 2. The analysis was based on segmented cross-sectional SEM images, as shown in Fig. S2. Overall, the Ti-rich phase area fraction increased with higher dealloying temperature and longer dealloying time. The Ti-rich phase area fractions of samples dealloyed at 460 °C were much higher than those of samples dealloyed at 400 °C, and the area fractions did not increase after dealloying at 460 °C for 7.5 min. The area fraction indicates that dealloying finished within a shorter time after dealloying at 460 °C than at lower temperatures; the relatively constant area fraction indicates that there was limited dealloying, and the formation of the larger globular ligament is likely driven by a coarsening mechanism, which occurred at the later stage of the process. Note that coarsening could have occurred with dealloying at the same time at the later stage. As shown in EXAFS analysis of the $Ti_{30}Cu_{70}$-460C-30 min sample, a globular structure can be found, and residual Cu still exists within parent alloy. Such coarsening was observed in samples with different parent alloy compositions under a longer heat-treatment time. The globular ligament was observed in samples with Ti concentration = 10–50 at.%, but became less obvious with an increasing Ti concentration in the parent alloy. This can be explained by the fact that the dealloying rate decreases with higher Ti in the parent alloy composition, so that after the same dealloying time, coarsening phenomena were more prominent in samples dealloyed from samples with a lower Ti concentration in the parent alloys. The dealloying rate variation with the parent alloy composition match with XPD results, which will be discussed in the later section.

The EXAFS analysis further confirmed that 460 °C is sufficiently high to fully dealloy the parent alloy films within 30 min. The EXAFS spectra are shown in Fig. S5. The fitting results of the EXAFS at Ti and Cu K-edges for the $Ti_{30}Cu_{70}$-340C-30, $Ti_{30}Cu_{70}$-400C-30, and $Ti_{30}Cu_{70}$-460C-30 specimens are summarized in Table 1. For the $Ti_{30}Cu_{70}$-340C-30 and $Ti_{30}Cu_{70}$-400C-30 samples, the first and second shells in Ti XAS were fitted well by Ti-O, Ti-Cu, and Ti-Ti paths, while only Ti-O and Ti-Ti paths could fit $Ti_{30}Cu_{70}$-460C-30. The intensity of the Ti-Cu peak in radial distribution functions corresponds to the coordination number (CN) of Ti-Cu bonds, which gradually decreased from 2.0 in $Ti_{30}Cu_{70}$-340C-30 to nearly zero in $Ti_{30}Cu_{70}$-460C-30. The Cu-Ti path in the Cu K-edge EXAFS showed a consistent decreasing trend, as summarized in Table 1. The gradual loss of the Ti-Cu peak indicates that the dealloying of Ti-Cu into the Ti and Cu_xMg phases was complete in the $Ti_{30}Cu_{70}$-460C-30 sample. Although the first shell (Ti-O) was fitted in each sample, the majority of samples were not oxidized, as shown by XANES in Fig. S5. Such a small amount of titanium oxides may be attributed to exposing the samples to ambient conditions. Note that during dealloying, morphological evolution started with a partial dissolution of the dissolving element Cu from the parent alloy. The evolution continues with Cu dissolution. Even after the Cu has been completely dissipated as confirmed by EXAFS, the coarsening process may continue, which drives globular Ti structure formation.

Table 1
The structural parameters for the $Ti_{30}Cu_{70}$-340C-30, $Ti_{30}Cu_{70}$-400C-30, and $Ti_{30}Cu_{70}$-460C-30 samples were obtained from Cu and Ti K-edge EXAFS data.

Sample	Shell	Coordination number	Bond length (Å)
Cu foil	Cu-Cu	12	2.54±0.01
$Ti_{30}Cu_{70}$-340C-30	Cu-Cu	3.1±0.8	2.46±0.02
	Cu-Ti	2.0±1.0	2.69±0.10
	Cu-Mg	4.9±1.1	2.79±0.04
$Ti_{30}Cu_{70}$-400C-30	Cu-Cu	2.8±0.6	2.47±0.10
	Cu-Ti	1.8±0.8	2.71±0.09
	Cu-Mg	4.7±0.9	2.79±0.10
$Ti_{30}Cu_{70}$-460C-30	Cu-Cu	2.8±1.6	2.48±0.02
	Cu-Mg	2.7±0.5	2.87±0.03
Ti foil	Ti-Ti	6	2.87±0.01
	Ti-Ti	6	2.93±0.01
$Ti_{30}Cu_{70}$-340C-30	Ti-O	1.1±0.5	2.04±0.07
	Ti-Cu	2.1±0.9	2.70±0.10
	Ti-Ti	3.7±1.6	2.97±0.09
$Ti_{30}Cu_{70}$-400C-30	Ti-O	0.9±0.4	2.08±0.08
	Ti-Cu	1.4±1.5	2.71±0.09
	Ti-Ti	5.3±1.6	2.97±0.06
$Ti_{30}Cu_{70}$-460C-30	Ti-O	0.9±0.1	2.10±0.17
	Ti-Ti	5.3±0.5	2.94±0.04

The Ti ligament coarsening is generally analyzed by fitting a power law between ligament size (d) and dealloying time (t) with the equation below:

$$d^n \sim t$$

where, the n values (n = 1–4) correspond to different transport mechanisms that control ligament coarsening: n = 1 corresponds to viscous flow of amorphous materials, n = 2 corresponds to evaporation and condensation mechanisms, n = 3 corresponds to volume diffusion, and n = 4 corresponds to surface diffusion [21,65]. All the mechanisms are driven by reduction of the surface free energy *via* material transport from high surface curvature (high diffusion potential) to low surface curvature (low diffusion potential) regions. However, due to the limited dealloying time and temperature, the quantitative fitting of ligament size with a power law is challenging, as summarized in Fig. S6. Here, we qualitatively discussed the coarsening mechanism.

In the LMD and ASD coarsening studies by experiments and Monte Carlo simulations [33,66], surface diffusion was determined as the mechanism of coarsening. In thin-film SSMD, since Ti and Mg are immiscible with each other, volume diffusion-driven Ti coarsening by diffusion of Ti atoms through the Mg-Cu lattice is limited, and surface diffusion-driven coarsening is most plausible here. In addition, the ligament size generated by the dealloying process in LMD and ASD is linearly correlated with the inverse homologous dealloying temperature on a log-log scale, which is calculated by dividing the melting point of the remaining element by the dealloying temperature [46]. The correlation was based on surface mobility-driven coarsening in dealloyed materials, which scales with homologous temperature [67]. Here, with an inverse homologous temperature of 3.62 (dealloying temperature was 460 °C), we obtained a ligament size of ~30 nm. The log-log model fits the data here for the Ti ligament size *vs.* the inverse homologous dealloying temperature in thin-film SSMD, further indicating that surface diffusion could be the dominant mechanism for coarsening in this study.

3.3. Structural and chemical evolution

To analyze the crystalline phase evolution, we conducted a systematic XRD measurement on Ti_xCu_{1-x} (x = 10–90 at.% with a 10% increment) both in the pristine state and in the dealloying states. The samples in the dealloyed states were dealloyed by Mg at 340, 400, and 460 °C from 7.5 min to 60 min. In the pristine samples, only a Mg crystalline phase was detected, and no diffraction peaks from any TiCu intermetallic phases were observed, indicating that the Ti_xCu_{1-x} parent alloy films are amorphous. An amorphous structure is commonly reported in literature for films prepared by sputtering deposition [68]. The XRD results of pristine sample were summarized in Fig. S3(a). In the dealloyed samples, three crystal phases, Ti, Cu_2Mg, and $CuMg_2$, were identified. A small amount of unreacted Mg was identified in the $Ti_{90}Cu_{10}$-460C-30 sample. The representative raw diffraction data are shown in Fig. S3(b), and the intensities of their strongest diffraction peaks are summarized in Fig. 3. Other diffraction peaks from Ti, Cu_2Mg, and $CuMg_2$ phases are summarized in Figs. S7–S9. The dealloying rate variation and phase transformation with parent alloy composition, dealloying time, and dealloying temperature are discussed below.

Dealloying rates are faster when more of the interdiffusing element, Cu, is present in the Ti-Cu parent alloy. At a low dealloying temperature (340 °C), the diffraction of Cu_2Mg and $CuMg_2$ can only be detected from samples with at least 60 at.% Cu in the parent alloy. Only at higher dealloying temperatures can diffraction of Cu_2Mg and $CuMg_2$ be gradually detected when at least 30 at.% Cu is present in the parent alloy.

The $CuMg_2$ phase transforms to Cu_2Mg when dealloying at higher temperatures or for longer times. In samples dealloyed from $Ti_{10}Cu_{90}$ and $Ti_{20}Cu_{80}$ with sufficient Cu in the parent alloy, at a lower dealloying temperature or for a shorter dealloying time, a $CuMg_2$ diffraction signal was detected. After dealloying at a higher temperature and for a longer time, the intensity of the diffraction signal from the $CuMg_2$ phase decreases and that from the Cu_2Mg phase increases. With insufficient Cu in the parent alloy, such as $Ti_{30}Cu_{70}$ and $Ti_{40}Cu_{60}$ samples, both $CuMg_2$ and Cu_2Mg diffraction signals can be detected. This phase transition and distribution are consistent with the results from prior studies of interdiffusion between Cu and Mg [69,70]. Dai et al. reported that the activation energy of $CuMg_2$ intermetallic phase growth was lower than that of the Cu_2Mg phase, and both intermetallic phases were present after interdiffusion at 460 °C. Arcot et al. reported a phase transformation from $CuMg_2$ to Cu_2Mg as long as the heating temperature was above 380 °C and there was an excess amount of Cu in the interdiffusion system [69].

The Cu_2Mg and $CuMg_2$ phases crystallized first, followed by the Ti phase. In the $Ti_{10}Cu_{90}$ and $Ti_{20}Cu_{80}$ samples, diffraction of crystalline Cu_2Mg and $CuMg_2$ generated by dealloying can be detected at the initial stage, such as at a lower dealloying temperature or with a shorter dealloying time, but no Ti diffraction signal was detected. Only at the later dealloying stage could diffraction of the Ti phase be detected. This may be explained by the activation energy of Cu_xMg interdiffusion being lower than that of Ti phase crystallization [70,71]. Therefore, the dealloying and surface reorganization of Ti could occur prior to the Ti crystallization process. Alternatively, this observation may indicate a suppression of the phase formation related to the thin film geometry in this study. Literature showed that most compound phases predicted by the equilibrium phase diagram may not occur in thin-film diffusion couples, due to their kinetic instability and interfacial reaction barriers [72]. Thus, the crystallization process may be suppressed during thin-film SSMD, and corresponding phase formation could be different compared to LMD and SMD in the bulk structures. In addition to the kinetic effect, literatures also provide alternative explanation based on thermodynamics, related to the thin-film geometry, such as (1) a nucleation barrier may be present to prevent the formation of a given phase in a diffusion couple [73], (2) lower diffusion temperature results in that forming these phases are thermodynamically impossible [74].

Note that although the Ti composition threshold which supports the formation of Cu_xMg and Ti phases increases with decreasing of the dealloying temperature, it does not imply a temperature-dependent parting limit. The temperature dependent behavior here only indicates the intermediate dealloying process at a specific dealloying temperature after a limited amount of dealloying time due to kinetic limitations, and thus does not correspond to the intrinsic parting limit of the system. Only fully dealloyed samples should be used for parting limit analysis, which will be further discussed in the later section.

Compared to the Cu_xMg phase evolution, the Ti phase evolution was challenging to be systematically resolved by XRD in the transmission mode. For selected samples, the potential presence of the intermediate TiCu phases were thus analyzed by Grazing-Incidence Wide-angle X-ray scattering (GIWAXS), shown in Fig. S4. In $Ti_{30}Cu_{70}$ samples dealloyed at 460 °C for 7.5 and 30 min, the Ti phase evolved from the amorphous parent alloy Ti_xCu_{1-x} to a crystalline TiCu alloy, then to the dealloyed crystal Ti phase. In samples dealloyed from different compositions of parent alloys ($Ti_{30}Cu_{70}$-460C-30, $Ti_{60}Cu_{40}$-460C-30, $Ti_{70}Cu_{30}$-460C-30, $Ti_{80}Cu_{20}$-460C-30), no TiCu crystalline phase was detected, which differs from the predictions based on the Ti-Cu phase diagram. Such difference may be explained by the diffusion process during the dealloying.

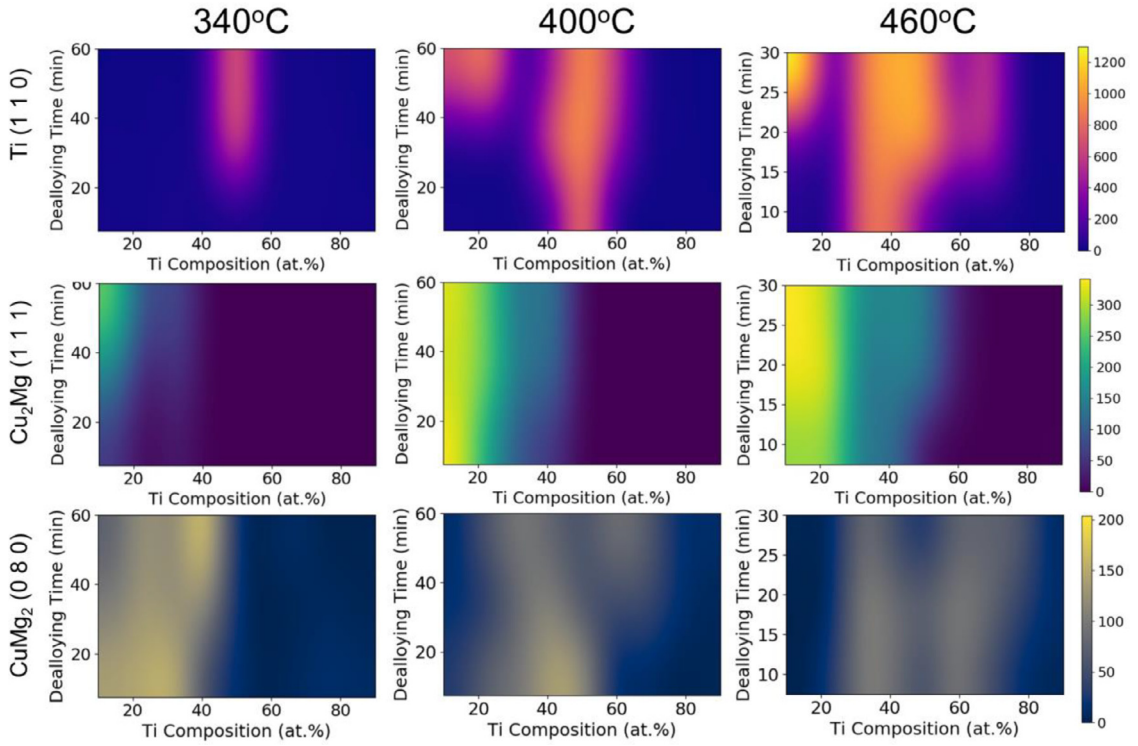

Fig. 3. The intensity of the Ti, Cu_2Mg, and $CuMg_2$ diffraction peaks from Ti_xCu_{1-x} (x = 10–90 at.% with a 10% increment) dealloyed by Mg at 340, 400, and 460 °C from 7.5 min to 60 min.

During dealloying, the Ti_xCu_{1-x} alloy composition continues to vary while the Cu is being removed from the alloy by Mg. If the crystallization of the Ti_xCu_{1-x} parent alloy and its dealloyed states is slower than the phase separation of the Ti and Cu driven by the solid-state solvent of Mg, fewer intermetallic compounds will be formed as a byproduct of the dealloying. Interestingly, here, only the most stable TiCu phase was detected as an intermediate crystalline phase (see Fig. S4, $Ti_{30}Cu_{70}$-460C-7.5 min), which also disappeared upon longer dealloying. In the study of Ti-Cu interdiffusion, Laik et al. has determined that the TiCu has the most negative value for heat of formation, and it is expected to form first at the diffusion zone between Ti and Cu [75]. The TiCu phase has been determined as the most stable phase out of seven stable and five metastable compound in Ti-Cu system [76]. The previously mentioned phase suppression driven by either thermodynamics or kinetics due to the thin-film geometry also explained the discrepancy of phase formation with phase diagram [72–74]. This observation critically illustrates the difference between the phase-separation process driven by the simple heat-treatment of the alloy (in the absence of a solvent), *vs.* the solid-state dealloying induced by a solvent, and the additional thermodynamic and kinetic interplay between these two.

Although the systematic XRD and GIWAXS analysis characterized the crystalline phases in dealloying, the evolution of the amorphous phase may also be present. Therefore, we conducted EXAFS analysis to complement the XRD characterization and analyzed the dealloying transition in Ti_xCu_{1-x} (x = 20–90 at.% with a 20 at.% increment) dealloyed by Mg at 460 °C for 30 min. The EXAFS analysis was also helpful to discern certain anomalous XRD results, such as the Ti phase in $Ti_{20}Cu_{80}$-460-30. The radial distribution functions of the EXAFS at the Cu and Ti K-edges are shown in Fig. 4, and their structural parameters at the Cu and Ti K-edge EXAFS are summarized in Table 2.

In the $Ti_{20}Cu_{80}$-460C-30, $Ti_{40}Cu_{60}$-460C-30, and $Ti_{60}Cu_{40}$-460C-30 samples, only Ti-O and Ti-Ti paths were fitted for the first and second shells in the Ti EXAFS analysis, respectively. The lack of the Ti-Cu path indicated that the parent alloys were fully dealloyed. Similarly, only Cu-Cu and Cu-Mg paths were fitted in the Cu EXAFS analysis, and no Cu-Ti paths were fitted. In contrast, in the $Ti_{80}Cu_{20}$-460C-30 sample, Cu-Cu, Cu-Ti, and Cu-Mg paths were fitted for the first and second shells, indicating that the sample was not fully dealloyed, and therefore, non-dealloyed Ti-Cu remained.

Table 2
The structural parameters for Ti_xCu_{1-x} (x = 20–90 at.% with a 20 at.% increment) dealloyed by Mg at 460 °C for 30 min, obtained from Cu and Ti K-edge EXAFS data.

Sample	Shell	Coordination number	Bond length (Å)
Cu foil	Cu-Cu	12	2.54±0.01
$Ti_{20}Cu_{80}$-460C-30	Cu-Cu	3.5±0.9	2.48±0.01
	Cu-Mg	2.9±0.3	2.90±0.03
$Ti_{40}Cu_{60}$-460C-30	Cu-Cu	2.5±0.4	2.47±0.02
	Cu-Mg	2.8±0.2	2.88±0.03
$Ti_{60}Cu_{40}$-460C-30	Cu-Cu	2.8±0.9	2.49±0.01
	Cu-Mg	3.4±0.5	2.80±0.08
$Ti_{80}Cu_{20}$-460C-30	Cu-Cu	1.4±0.5	2.54±0.21
	Cu-Ti	0.9±0.6	2.74±1.91
	Cu-Mg	4.9±0.7	2.77±0.50
$Ti_{90}Cu_{10}$-460C-30	Cu-Cu	3.2±2.9	2.43±0.01
	Cu-Ti	1.9±1.4	2.64±0.29
Ti foil	Ti-Ti	6	2.87±0.01
	Ti-Ti	6	2.93±0.01
$Ti_{20}Cu_{80}$-460C-30	Ti-O	0.8±0.3	1.98±0.05
	Ti-Ti	6.4±1.1	2.94±0.06
$Ti_{40}Cu_{60}$-460C-30	Ti-O	0.6±0.1	2.10±0.12
	Ti-Ti	4.4±0.4	2.92±0.02
$Ti_{60}Cu_{40}$-460C-30	Ti-O	1.3±0.3	2.09±0.12
	Ti-Ti	4.0±0.8	2.96±0.05
$Ti_{80}Cu_{20}$-460C-30	Ti-O	1.2±0.8	2.09±0.11
	Ti-Cu	0.3±1.3	2.74±1.91
	Ti-Ti	4.5±1.1	2.95±0.02
$Ti_{90}Cu_{10}$-460C-30	Ti-O	1.4±0.7	2.09±0.10
	Ti-Cu	0.6±1.6	2.64±0.29
	Ti-Ti	3.7±2.4	2.93±0.07

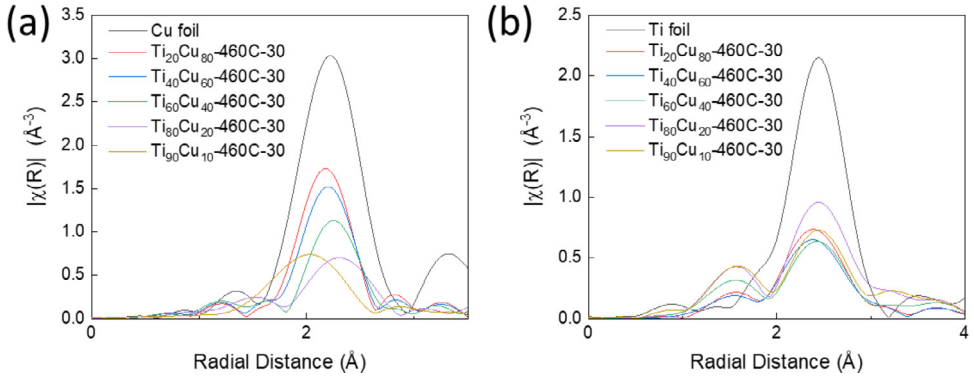

Fig. 4. The radial distribution functions of the EXAFS results for Ti_xCu_{1-x} samples (x = 20–90 at.% with a 20 at.% increment) dealloyed by Mg at 460 °C for 30 min.

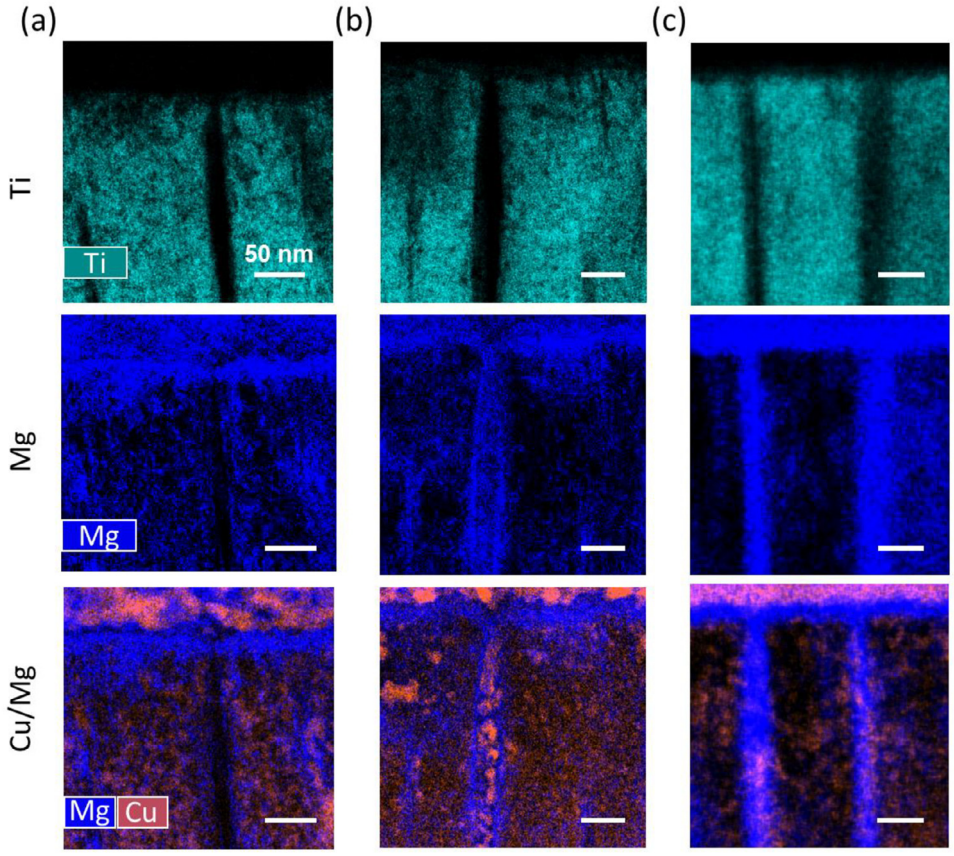

Fig. 5. Ti, Mg and Cu/Mg EDX maps of the (a) $Ti_{60}Cu_{40}$-460C-30, (b) $Ti_{70}Cu_{30}$-460C-30 and (c) $Ti_{80}Cu_{20}$-460C-30 samples. All of the scale bars correspond to 50 nm.

In the $Ti_{90}Cu_{10}$-460C-30 sample, Cu-Ti and Cu-Cu paths were fitted for the first shell, and no Cu-Mg was fitted. The EXAFS fitting indicated that dealloying could not progress through the entire film when the Cu concentration in the parent alloy was below 20 at. %, which is consistent with the XRD results and STEM/EDX mapping. This aspect will be discussed in a later section.

In addition, the fitting result for the $Ti_{20}Cu_{80}$-460C-30 sample is similar to that for the $Ti_{40}Cu_{60}$-460C-30 and $Ti_{60}Cu_{40}$-460C-30 samples, indicating similar local environments. Therefore, only the crystal structure in $Ti_{20}Cu_{80}$-460C-30 is different from that of the other samples, but dealloying is complete in this sample. The abnormal crystal structure in the $Ti_{20}Cu_{80}$-460C-30 and $Ti_{30}Cu_{70}$-400C-60 samples may be attributed to sample variation or the presence of oxygen during the sample preparation process. Note that the EXAFS analysis showed that the local structure of these samples follows the overall trend of all samples.

3.4. Parting limit in thin-film SSMD of Ti-Cu system

The parting limit is a composition threshold; when the concentration of the interdiffusing elements concentration in the parent alloy is below this threshold, dealloying cannot occur beyond the first few atomic layers [44]. When the concentration of the interdiffusing elements is above the parting limit, an atomic-scale network/chain of the interdiffusing elements can support continuous

dissolution into the entire structure. This dissolution corresponds to a percolation dissolution mechanism for dealloying [44]. The theoretical site percolations for FCC and HCP lattices were determined to be ~20 at.%, and for the BCC lattice, they were determined to be ~24.5 at.% [33,77]. In the ASD experiments, although few systems, such as the Cu-Zn system, show a parting limit close to the theoretical percolation limit of ~20 at.%, common systems, such as Au-Ag and Au-Cu, show a much higher parting limit of ~55 at.%. Artymowicz et al. explained this difference in terms of a high-density percolation network in which the percolation chain of the interdiffusing elements needs to be wide enough for dealloying to progress through the bulk structure [45]. In addition, the smoothing effect of remaining element surface diffusion during dealloying causes the parting limit to be higher than the theoretical site percolation threshold [33].

In the SSMD Ti-Cu system, diffraction signals from the Ti, Cu_2Mg, and $CuMg_2$ phases can be detected from samples dealloyed from parent alloys with more than 20 at.% Cu, as shown in Fig. 3. In addition, in the EXAFS fitting analysis, the first shell Ti-Cu can only be fitted in samples dealloyed from the parent alloy with less than 30 at.% Cu. Considering that dealloying at 460 °C for 30 min is enough to fully dealloy samples with other compositions, the $Ti_{80}Cu_{20}$ sample cannot be fully dealloyed, so the parting limit should be above 20 at.% in Ti-Cu thin-film SSMD.

To further analyze the precise parting limit of thin-film SSMD in the Ti-Cu system, a high-resolution STEM/EDX analysis of $Ti_{60}Cu_{40}$-460C-30, $Ti_{70}Cu_{30}$-460C-30, and $Ti_{80}Cu_{20}$-460C-30 was conducted, as shown in Fig. 5. A bicontinuous Ti/Mg distribution is identified at the center region of the film/columnar structure in the $Ti_{60}Cu_{40}$-460C-30 sample. A bicontinuous Ti/Mg distribution is visible only at the boundary region of the columnar structure in the $Ti_{70}Cu_{30}$-460C-30 sample, and no clear Ti/Mg feature can be identified in the $Ti_{80}Cu_{20}$-460C-30 sample. In addition, the Mg distribution in the $Ti_{70}Cu_{30}$-460C-30 and $Ti_{80}Cu_{20}$-460C-30 samples also indicates limited interdiffusion between Mg and Cu. With decreasing Cu concentration in the parent alloy, more Mg is distributed along the boundaries of the columnar structure, indicating that Mg cannot diffuse into the structure, as shown in Fig. 5. This observation is consistent with the percolation theory, that when the concentration of the interdiffusing element (Cu) is below the parting limit, no chains of Cu can pass through the sample, so Mg cannot interdiffuse with Cu into the samples. Therefore, the parting limit in thin-film SSMD Ti-Cu was determined to be 30–40 at.%.

The parting limit in thin-film SSMD Ti-Cu is close to the reported parting limit of 30–40 at.% in LMD for a Ti-Ta parent alloy. However, if simply determining the parting limit by XRD or EXAFS analysis, such a threshold value can be lower. In XRD analysis, the diffraction peak from $CuMg_2$ and Ti phases can also be detected in the $Ti_{70}Cu_{30}$-460C-30 sample, which is likely due to the limited dealloying at the surface but not dealloying through the bulk structure. This is related to the different crystal structures in the bulk LMD samples and the thin-film SSMD samples. The samples in LMD experiments have large grains with a size of 50–100 μm; in thin-film SSMD, the parent alloy is amorphous, but there are a large number of columnar structures with diameters less than 100 nm along the dealloying direction. The dealloyed samples are shown in Fig. 5, and the pristine parent alloy is shown in Fig. S10. Columnar structures are commonly found in sputtering deposited thin films; the presence of these columnar structures can introduce free surfaces and therefore provide low coordinated sites, which may enable dealloying at the surface of these columnar structures. Dissolution of Cu into Mg through the boundary of these columnar structures can be identified by overlapping the Cu and Mg EDX mappings, whereas a large amount of Cu colocalizes with Mg at the boundary of the columnar structures, as shown in Fig. 5.

4. Conclusions

In this work, we systematically analyzed the kinetics of SSMD thin films prepared from Ti-Cu parent alloys with a Mg solvent. Processing parameters, including the parent alloy composition, dealloying time, and dealloying temperature, were analyzed. The parent alloy covered the composition range from 10 at.% Ti to 90 at.% Ti.

The morphological transitions of the Ti structure, from globular to lamellar and bicontinuous shapes, with increasing Ti concentration in the parent alloy were identified. The dealloying and coarsening at different dealloying stages was identified, whereas coarsening drove formation of the large globular structure. With increasing Ti concentration in the parent alloy, the Ti ligament size distribution became narrower, and the corresponding average ligament size decreased. Synchrotron XRD and EXAFS were applied to reveal the structural and chemical evolution during thin-film SSMD. In thin-film SSMD of Ti-Cu parent alloy, crystalline $CuMg_2$, Cu_2Mg, and Ti were sequentially detected.

The delay in phase formation indicates a potential phase suppression, which may be caused by interfacial reaction barrier control kinetics, thermodynamic nucleation barrier, or a lower diffusion temperature. Because of the additional factors such as different crystallization temperature and higher surface energies, equilibrium phase diagrams for bulk materials that are commonly used as design criteria for LMD and SMD in bulk structure, may not be accurate when screening and identifying thin-film SSMD systems. Additional criteria and factors that can alter or dominate the thermodynamics and kinetics in a thin-film geometry need to be considered. Additionally, the potential phase suppression also opens up opportunities for applying the thin-film SSMD in other systems, where deleterious intermetallic phase formation may need to be prevented. For instance, some brittle intermetallic phases could form during the dealloying process; by kinetically or thermodynamically suppressing or delaying the formation of these phases, a broader range of SSMD systems could be explored in thin-film geometries that may not be possible in bulk.

The phase transformations forming crystalline $CuMg_2$ and Cu_2Mg with increasing dealloying temperature and time were analyzed. With the support of EXAFS analysis, the dependence of the dealloying progress on dealloying temperature was analyzed. Dealloying at 460 °C for 30 min was sufficient to fully dealloy Ti-Cu parent alloy thin-films with a thickness of 400 nm. By analyzing the diffraction peak intensities as functions of parent alloy composition, we determined that the dealloying rate increased as the amount of interdiffusing element, Cu, in the parent alloys increased.

The parting limit, a composition threshold of the interdiffusing elements below which dealloying cannot occur below the surface, was collectively determined by XRD, EXAFS, cross-sectional SEM and STEM/EDX mapping. In dealloyed samples, the Ti-Cu residual bonds were fitted by EXAFS and no dealloyed phases were identified by XRD, indicating that the parting limit was above 20 at.% Cu. High-resolution EDX mapping confirmed the distribution of a bicontinuous Ti structure generated by dealloying and the distribution of the solvent Mg, which identified the parting limit in the SSMD thin films of Ti-Cu as 30–40 at. %. In this study, we explored the morphological, structural, and chemical evolution of thin-film SSMD with respect to parent alloy composition, dealloying temperature, and dealloying time. This work furthered our understanding of the processing conditions vs. the structure, chemistry, and morphology of the systems. The results laid groundwork for future material design by thin-film SSMD.

Declaration of Competing Interest

The authors declare that they have no known competing financial interests or personal relationships that could have appeared to influence the work reported in this paper.

CRediT authorship contribution statement

Chonghang Zhao: Investigation, Data curation, Formal analysis, Conceptualization, Methodology, Validation, Visualization, Writing – original draft, Writing – review & editing. **Lin-Chieh Yu:** Conceptualization, Formal analysis, Data curation, Visualization, Writing – original draft, Writing – review & editing. **Kim Kisslinger:** Data curation, Investigation, Writing – review & editing. **Charles Clark:** Formal analysis, Writing – review & editing. **Cheng-Chu Chung:** Formal analysis, Visualization, Writing – review & editing. **Ruipeng Li:** Data curation, Formal analysis, Investigation, Methodology, Writing – review & editing. **Masafumi Fukuto:** Formal analysis, Methodology, Writing – review & editing. **Ming Lu:** Formal analysis, Writing – review & editing. **Jianming Bai:** Formal analysis, Writing – review & editing. **Xiaoyang Liu:** Formal analysis, Writing – review & editing. **Hui Zhong:** Formal analysis, Data curation, Writing – review & editing. **Mingzhao Liu:** Supervision, Methodology, Writing – review & editing. **Sanjit Ghose:** Methodology, Supervision, Writing – review & editing. **Yu-chen Karen Chen-Wiegart:** Investigation, Conceptualization, Data curation, Funding acquisition, Methodology, Project administration, Resources, Supervision, Writing – review & editing.

Acknowledgments

This material is based on work supported by the National Science Foundation under Grant No. DMR-1752839. Karen Chen-Wiegart acknowledges the support provided *via* the Faculty Early Career Development Program (CAREER) program and the Metals and Metallic Nanostructures Program of the National Science Foundation. This research used resources, the Beamline for Materials Measurement (BMM, 6-BM), the X-ray Powder Diffraction beamline (XPD, 28-ID-2) and the Complex Materials Scattering beamline (CMS, 11-BM), of the National Synchrotron Light Source II, a U.S. Department of Energy (DOE) Office of Science User Facility operated for the DOE Office of Science by Brookhaven National Laboratory under Contract No. DE-SC0012704. This research used the Electron Microscopy, Materials Synthesis and Characterization, and Nanofabrication Facilities of the Center for Functional Nanomaterials (CFN), which is a U.S. DOE Office of Science User Facility, at Brookhaven National Laboratory under Contract No. DE-SC0012704. Chonghang Zhao and Karen Chen-Wiegart thank the Joint Photon Science Institute at Stony Brook University, which provides partial support for Chonghang Zhao *via* a student fellowship jointly proposed by Karen Chen-Wiegart as principal investigator (PI) and Yong Chu as co-PI and Juergen Thieme and Wah-Keat Lee as collaborators.

The authors are grateful to Dr. Bruce Ravel (National Institute of Standards and Technology), a scientist at the BMM beamline, for his expertise and support on XAS characterization as well as his insights into data analysis and scientific interpretation. We appreciate the support provided by the CFN staff, Fernando Camino and Gwen Wright, for access to and training on the FIB-SEM and SEM/EDX. We acknowledge the support of data collection and preliminary analysis during the XPD beamtime provided by the Chen-Wiegart group members, Lijie Zou and Qingkun Meng. Lin-Chieh Yu thanks Yang Liu from Prof. Anatoly Frenkel's group at Stony Brook University and Brookhaven National Laboratory for helpful advice on the EXAFS analysis, as well as Prof. Anatoly Frenkel for helpful discussions and the XAFS 2020 Short Course on X-ray Absorption Fine Structure. The authors also thank insightful comments from reviewers.

Supplementary materials

Supplementary material associated with this article can be found, in the online version, at doi:10.1016/j.actamat.2022.118433.

References

[1] X. Liu, et al., Power generation by reverse electrodialysis in a single-layer nanoporous membrane made from core-rim polycyclic aromatic hydrocarbons, Nat. Nanotechnol. 15 (2020) 307–312, doi:10.1038/s41565-020-0641-5.
[2] B. Zugic, et al., Dynamic restructuring drives catalytic activity on nanoporous gold-silver alloy catalysts, Nat. Mater. 16 (2017) 558–564, doi:10.1038/nmat4824.
[3] S. Shi, Y. Li, B.N. Ngo-Dinh, J. Markmann, J. Weissmuller, Scaling behavior of stiffness and strength of hierarchical network nanomaterials, Science (New York, N.Y.) 371 (2021) 1026–1033, doi:10.1126/science.abd9391.
[4] J. Erlebacher, M.J. Aziz, A. Karma, N. Dimitrov, K. Sieradzki, Evolution of nanoporosity in dealloying, Nature 410 (2001) 450–453, doi:10.1038/35068529.
[5] L.F. Zou, et al., Atomic-scale phase separation induced clustering of solute atoms, Nat. Commun. 11 (2020), doi:10.1038/s41467-020-17826-w.
[6] L.L. Huang, et al., Shape regulation of high-index facet nanoparticles by dealloying, Science 365 (2019) 1159, doi:10.1126/science.aax5843.
[7] C. Zhu, et al., Toward digitally controlled catalyst architectures: hierarchical nanoporous gold *via* 3D printing, Sci. Adv. 4 (2018), doi:10.1126/sciadv.aas9459.
[8] A. Wittstock, V. Zielasek, J. Biener, C.M. Friend, M. Baumer, Nanoporous gold catalysts for selective gas-phase oxidative coupling of methanol at low temperature, Science 327 (2010) 319–322, doi:10.1126/science.1183591.
[9] A. Pavlisic, et al., Atomically resolved dealloying of structurally ordered Pt nanoalloy as an oxygen reduction reaction electrocatalyst, ACS Catal. 6 (2016) 5530–5534, doi:10.1021/acscatal.6b00557.
[10] A.A. El-Zoka, et al., Enabling near-atomic-scale analysis of frozen water, Sci. Adv. 6 (2020), doi:10.1126/sciadv.abd6324.
[11] J.T. Zhang, C.M. Li, Nanoporous metals: fabrication strategies and advanced electrochemical applications in catalysis, sensing and energy systems, Chem. Soc. Rev. 41 (2012) 7016–7031, doi:10.1039/c2cs35210a.
[12] W.L. An, et al., Scalable synthesis of ant-nest-like bulk porous silicon for high-performance lithium-ion battery anodes, Nat. Commun. 10 (2019), doi:10.1038/s41467-019-09510-5.
[13] Y.Q. Li, et al., Dual-phase nanostructuring of layered metal oxides for high-performance aqueous rechargeable potassium ion microbatteries, Nat. Commun. 10 (2019), doi:10.1038/s41467-019-12274-7.
[14] Q. Chen, K. Sieradzki, Spontaneous evolution of bicontinuous nanostructures in dealloyed Li-based systems, Nat. Mater. 12 (2013) 1102–1106, doi:10.1038/nmat3741.
[15] C.H. Zhao, et al., Imaging of 3D morphological evolution of nanoporous silicon anode in lithium ion battery by X-ray nano-tomography, Nano Energy 52 (2018) 381–390, doi:10.1016/j.nanoen.2018.08.009.
[16] N. Badwe, et al., Decoupling the role of stress and corrosion in the intergranular cracking of noble-metal alloys, Nat. Mater. 17 (2018) 887–893, doi:10.1038/s41563-018-0162-x.
[17] J. Snyder, T. Fujita, M.W. Chen, J. Erlebacher, Oxygen reduction in nanoporous metal - ionic liquid composite electrocatalysts, Nat. Mater. 9 (2010) 904–907, doi:10.1038/nmat2878.
[18] T. Fujita, et al., Atomic origins of the high catalytic activity of nanoporous gold, Nat. Mater. 11 (2012) 775–780, doi:10.1038/nmat3391.
[19] J.H. Han, et al., Vapor phase dealloying: a versatile approach for fabricating 3D porous materials, Acta Mater. 163 (2019) 161–172, doi:10.1016/j.actamat.2018.10.012.
[20] Z. Lu, et al., Three-dimensional bicontinuous nanoporous materials by vapor phase dealloying, Nat. Commun. 9 (2018), doi:10.1038/s41467-017-02167-y.
[21] X. Liu, et al., Formation of three-dimensional bicontinuous structures *via* molten salt dealloying studied in real-time by *in situ* synchrotron X-ray nano-tomography, Nat. Commun. 12 (2021) 3441 3441, doi:10.1038/s41467-021-23598-8.
[22] T. Wada, K. Yubuta, A. Inoue, H. Kato, Dealloying by metallic melt, Mater. Lett. 65 (2011) 1076–1078, doi:10.1016/j.matlet.2011.01.054.
[23] T. Wada, et al., Bulk-nanoporous-silicon negative electrode with extremely high cyclability for lithium-ion batteries prepared using a top-down process, Nano Lett. 14 (2014) 4505–4510, doi:10.1021/nl501500g.
[24] C.H. Zhao, et al., Three-dimensional morphological and chemical evolution of nanoporous stainless steel by liquid metal dealloying, ACS Appl. Mater. Interfaces 9 (2017) 34172–34184, doi:10.1021/acsami.7b04659.
[25] T. Wada, H. Kato, Three-dimensional open-cell macroporous iron, chromium and ferritic stainless steel, Scr. Mater. 68 (2013) 723–726, doi:10.1016/j.scriptamat.2013.01.011.
[26] I.V. Okulov, et al., Nanoporous magnesium, Nano Res. 11 (2018) 6428–6435, doi:10.1007/s12274-018-2167-9.

[27] S.G. Yu, K. Yubuta, T. Wada, H. Kato, Three-dimensional bicontinuous porous graphite generated in low temperature metallic liquid, Carbon 96 (2016) 403–410, doi:10.1016/j.carbon.2015.09.093.

[28] M. Tsuda, T. Wada, H. Kato, Kinetics of formation and coarsening of nanoporous alpha-titanium dealloyed with Mg melt, J. Appl. Phys. 114 (2013) 113503-113501-113508, doi:10.1063/1.4821066.

[29] T. Wada, A.D. Setyawan, K. Yubuta, H. Kato, Nano- to submicro-porous beta-Ti alloy prepared from dealloying in a metallic melt, Scr. Mater. 65 (2011) 532–535, doi:10.1016/j.scriptamat.2011.06.019.

[30] L.J. Zou, et al., Designing multiscale porous metal by simple dealloying with 3D morphological evolution mechanism revealed *via* X-ray nano-tomography, ACS Appl. Mater. Interfaces 12 (2020) 2793–2804, doi:10.1021/acsami.9b16392.

[31] L.J. Zou, et al., 3D morphology of bimodal porous copper with nano-sized and micron-sized pores to enhance transport properties for functional applications, ACS Appl. Nano Mater. 3 (2020) 7524–7534, doi:10.1021/acsanm.0c01163.

[32] B. Gaskey, I. McCue, A. Chuang, J. Erlebacher, Self-assembled porous metal-intermetallic nanocomposites *via* liquid metal dealloying, Acta Mater. 164 (2019) 293–300, doi:10.1016/j.actamat.2018.10.057.

[33] I. McCue, B. Gaskey, P.A. Geslin, A. Karma, J. Erlebacher, Kinetics and morphological evolution of liquid metal dealloying, Acta Mater. 115 (2016) 10–23, doi:10.1016/j.actamat.2016.05.032.

[34] I. McCue, et al., Size effects in the mechanical properties of bulk bicontinuous Ta/Cu nanocomposites made by liquid metal dealloying, Adv. Eng. Mater. 18 (2016) 46–50, doi:10.1002/adem.201500219.

[35] I.V. Okulov, J. Weissmuller, J. Markmann, Dealloying-based interpenetrating-phase nanocomposites matching the elastic behavior of human bone, Sci. Rep. 7 (2017) 20–27, doi:10.1038/s41598-017-00048-4.

[36] S.H. Joo, et al., Beating thermal coarsening in nanoporous materials *via* high-entropy design, Adva. Mater. 32 (2020), doi:10.1002/adma.201906160.

[37] T. Wada, K. Yubuta, H. Kato, Evolution of a bicontinuous nanostructure *via* a solid-state interfacial dealloying reaction, Scr. Mater. 118 (2016) 33–36, doi:10.1016/j.scriptamat.2016.03.008.

[38] Y. Shi, L.X. Lian, Y. Liu, N.Y. Xing, A novel solid-state dealloying method to prepare ultrafine ligament nanoporous Ti, Appl. Phys. A Mater. Sci. Process. 125 (2019), doi:10.1007/s00339-019-2984-z.

[39] C.H. Zhao, et al., Design nanoporous metal thin films via solid state interfacial dealloying, Nanoscale 13 (2021), doi:10.1039/d1nr03709a.

[40] I. McCue, M.J Demkowicz, Alloy design criteria for solid metal dealloying of thin films, JOM 69 (2017) 2199–2205, doi:10.1007/s11837-017-2571-8.

[41] C.H. Zhao, et al., Bi-continuous pattern formation in thin films *via* solid-state interfacial dealloying studied by multimodal characterization, Mater. Horiz. 6 (2019) 1991–2002, doi:10.1039/c9mh00669a.

[42] Y.C.K. Chen-Wiegart, et al., Structural evolution of nanoporous gold during thermal coarsening, Acta Mater. 60 (2012) 4972–4981, doi:10.1016/j.actamat.2012.05.012.

[43] J. Erlebacher, Mechanism of coarsening and bubble formation in high-genus nanoporous metals, Phys. Rev. Lett. 106 (2011) 225504, doi:10.1103/PhysRevLett.106.225504.

[44] Q. Chen, K. Sieradzki, Mechanisms and morphology evolution in dealloying, J. Electrochem. Soc. 160 (2013) C226–C231, doi:10.1149/2.064306jes.

[45] D.M. Artymowicz, J. Erlebacher, R.C. Newman, Relationship between the parting limit for de-alloying and a particular geometric high-density site percolation threshold, Philosoph. Mag. 89 (2009) 1663–1693, doi:10.1080/14786430903025708.

[46] I. McCue, A. Karma, J. Erlebacher, Pattern formation during electrochemical and liquid metal dealloying, MRS Bull. 43 (2018) 27–34, doi:10.1557/mrs.2017.301.

[47] P. Haldar, A. Chatterjee, Extent of dissolution determines the structural similarity between dealloyed nanoporous materials synthesized at unrelated dissolution conditions, Acta Mater. 152 (2018) 186–198, doi:10.1016/j.actamat.2018.04.020.

[48] W.B. Andrews, K.L.M. Elder, P.W. Voorhees, K. Thornton, Effect of transport mechanism on the coarsening of bicontinuous structures: a comparison between bulk and surface diffusion, Phys. Rev. Mater. 4 (2020), doi:10.1103/PhysRevMaterials.4.103401.

[49] N. Mameka, K. Wang, J. Markmann, E.T. Lilleodden, J. Weissmuller, Nanoporous gold-testing macro-scale samples to probe small-scale mechanical behavior, Mater. Res. Lett. 4 (2016) 27–36, doi:10.1080/21663831.2015.1094679.

[50] P.A. Geslin, I. McCue, B. Gaskey, J. Erlebacher, A. Karma, Topology-generating interfacial pattern formation during liquid metal dealloying, Nat. Commun. 6 (2015) 8, doi:10.1038/ncomms9887.

[51] L.H. Lai, B. Gaskey, A. Chuang, J. Erlebacher, A. Karma, Topological control of liquid-metal-dealloyed structures, Nat. Commun. 13 (2022), doi:10.1038/s41467-022-30483-5.

[52] S.H. Joo, H. Kato, Transformation mechanisms and governing orientation relationships through selective dissolution of Ni *via* liquid metal dealloying from (FeCo)(x)Ni100-x precursors, Mater. Des. 185 (2020), doi:10.1016/j.matdes.2019.108271.

[53] S.H. Joo, H. Kato, Effect of dealloying rate on transformation behavior during liquid metal dealloying, J. Alloys Compd. 831 (2020), doi:10.1016/j.jallcom.2020.154733.

[54] F.M. Zhang, et al., Fabrication, formation mechanism and properties of three-dimensional nanoporous titanium dealloyed in metallic powders, J. Mater. Res. 32 (2017) 1528–1540, doi:10.1557/jmr.2017.19.

[55] I. McCue, E. Benn, B. Gaskey, J. Erlebacher, Dealloying and dealloyed materials, Annu. Rev. Mater. Res 46 (1) (2016) 263–286.

[56] Y.C.K. Chen-Wiegart, et al., 3D morphological evolution of porous titanium by X-ray micro- and nano-tomography, J. Mater. Res. 28 (2013) 2444–2452, doi:10.1557/jmr.2013.151.

[57] Y.C.K. Chen-Wiegart, S. Wang, I. McNulty, D.C. Dunand, Effect of Ag-Au composition and acid concentration on dealloying front velocity and cracking during nanoporous gold formation, Acta Mater. 61 (2013) 5561–5570, doi:10.1016/j.actamat.2013.05.039.

[58] Y.C.K. Chen-Wiegart, et al., *In situ* imaging of dealloying during nanoporous gold formation by transmission X-ray microscopy, Acta Mater. 61 (2013) 1118–1125, doi:10.1016/j.actamat.2012.10.017.

[59] H. Wu, T. Mayeshiba, D. Morgan, High-throughput *ab-initio* dilute solute diffusion database, Sci. Data 3 (2016), doi:10.1038/sdata.2016.54.

[60] A. O'Mara, A.E. King, J.C. Vickers, M.T.K. Kirkcaldie, ImageSURF: an ImageJ plugin for batch pixel-based image segmentation using random forests, J. Open Res. Softw. 5 (2017), doi:10.5334/jors.172.

[61] B. Munch, L. Holzer, Contradicting geometrical concepts in pore size analysis attained with electron microscopy and mercury intrusion, J. Am. Ceram. Soc. 91 (2008) 4059–4067, doi:10.1111/j.1551-2916.2008.02736.x.

[62] B. Ravel, M. Newville, ATHENA, ARTEMIS, HEPHAESTUS: data analysis for X-ray absorption spectroscopy using IFEFFIT, J. Synchrotron Radiat. 12 (2005) 537–541, doi:10.1107/s0909049505012719.

[63] J.J. Rehr, R.C. Albers, Theoretical approaches to x-ray absorption fine structure, Rev. Mod. Phys. 72 (2000) 621–654, doi:10.1103/RevModPhys.72.621.

[64] I. McCue, S.S. Xiang, K. Xie, M.J. Demkowicz, The effect of microstructure morphology on indentation response of Ta/Ti nanocomposite thin films, Metall. Mater. Trans. A Phys. Metall. Mater. Sci. 51 (2020) 5677–5690, doi:10.1007/s11661-020-05969-w.

[65] C. Herring, Effect of change of scale on sintering phenomena, J. Appl. Phys. 21 (1950) 301–303, doi:10.1063/1.1699658.

[66] Y. Li, B.N.D. Ngo, J. Markmann, J. Weissmueller, Topology evolution during coarsening of nanoscale metal network structures, Phys. Rev. Mater. 3 (2019), doi:10.1103/PhysRevMaterials.3.076001.

[67] C.P. Flynn, Why is diffusion in metals and on metal surfaces universal? J. Phys. Condens. Matter 18 (2006) S439–S445, doi:10.1088/0953-8984/18/16/s05.

[68] Y.L. Jeyachandran, et al., Properties of titanium thin films deposited by dc magnetron sputtering, Mater. Sci. Eng. A Struct. Mater. Prop. Microstruct. Process. 431 (2006) 277–284, doi:10.1016/j.msea.2006.06.020.

[69] B. Arcot, et al., Intermetallic formation in copper/magnesium thin-films - kinetics, nucleation and growth, and effect of interfacial oxygen, J. Appl. Phys. 76 (1994) 5161–5170, doi:10.1063/1.357231.

[70] J.H. Dai, et al., Diffusion kinetics in Mg-Cu binary system, J. Phase Equilibria Diffus. 36 (2015) 613–619, doi:10.1007/s11669-015-0417-z.

[71] T. Yamane, J. Ueda, Recrystallization of a cold rolled commercial pure titanium plate by isothermal annealing, Trans. Jpn. Inst. Metals 4 (1963) 242–244, doi:10.2320/matertrans1960.4.242.

[72] U. Gosele, K.N. Tu, Growth kinetics of planar binary diffusion couples: thin-film case versus bulk cases, J. Appl. Phys. 53 (1982) 3252–3260, doi:10.1063/1.331028.

[73] J.E.E. Baglin, F.M. d'Heurle, C.S. Peterson, Thin Film Interfaces and Interactions, 341, The Electrochemical Society, 1980.

[74] S.U. Campisano, Thin Film Phenomena-Interfaces and Interactions, 129, The Electrochemical Society, 1978.

[75] A. Laik, K. Bhanumurthy, G.B. Kale, B.P. Kashyap, Diffusion characteristics in the Cu-Ti system, Int. J. Mater. Res. 103 (2012) 661–672, doi:10.3139/146.110685.

[76] G. Ghosh, First-principles calculations of structural energetics of Cu-TM (TM = Ti, Zr, Hf) intermetallics, Acta Mater. 55 (2007) 3347–3374, doi:10.1016/j.actamat.2007.01.037.

[77] C.D. Lorenz, R. May, R.M. Ziff, Similarity of percolation thresholds on the HCP and FCC lattices, J. Stat. Phys. 98 (2000) 961–970, doi:10.1023/a:1018648130343.